



### **Science Arts & Métiers (SAM)**

is an open access repository that collects the work of Arts et Métiers Institute of Technology researchers and makes it freely available over the web where possible.

This is an author-deposited version published in: <https://sam.ensam.eu>  
Handle ID: <http://hdl.handle.net/10985/21464>

#### **To cite this version :**

M. DAOUD, Regis KUBLER, A. BEMOU, P. OSMOND, Arnaud POLETTE - Prediction of residual stress fields after shot-peening of TRIP780 steel with second-order and artificial neural network models based on multi-impact finite element simulations - Journal of Manufacturing Processes - Vol. 72, p.529-543 - 2021

Any correspondence concerning this service should be sent to the repository

Administrator : [scienceouverte@ensam.eu](mailto:scienceouverte@ensam.eu)



Prediction of residual stress fields after shot-peening of TRIP780 steel with second-order and artificial neural network models based on multi-impact finite element simulations

**M. Daoud<sup>1</sup>, R. Kubler<sup>2</sup>, A. Bemou<sup>1</sup>, P. Osmond<sup>3</sup>, A. Polette<sup>4</sup>**

<sup>1</sup> French Technological Research Institute for Materials, Metallurgy and Processes (IRT-M2P)  
4, rue Augustin Fresnel, 57070 Metz, France

<sup>2</sup> Arts et Metiers Institute of Technology, MSMP Laboratory, HESAM Université, 2 cours des  
Arts et Métiers, 13617 Aix-en-Provence, France

<sup>3</sup> Stellantis, 212 Boulevard Pelletier, 78955 Carrières-sous-Poissy

<sup>4</sup> Arts et Metiers Institute of Technology, LISPEN Laboratory, HESAM Université, 2 cours  
des Arts et Métiers, 13617 Aix-en-Provence, France

**Abstract:**

Shot-peening is a surface mechanical treatment widely employed to enhance the fatigue life of metallic components by introducing compressive surface residual stress fields. These fields are mainly impacted by the selection of the process parameters. The aim of this work is to propose a hybrid approach to conduct two predictive models: second-order model and feed-forward artificial neural network model. For this purpose, a 3D multiple-impacts finite element model coupled to a central composite design of experiments was employed. A parametric analysis was also conducted to investigate the effect of the shot diameter, the shot velocity, the coverage, and the impact angle on the induced residual stress profile within a TRIP780 steel. It was found that both predictive models predict with good agreement, the residual stress profile as a function of the process parameters and can be used in shot-peening optimization due to their responsiveness.

**Keywords:** *Shot-peening; Residual stresses; Finite element modeling; Second-order response surface model; Artificial neural network model*

**Nomenclature**

|       |   |
|-------|---|
| $a$   | Impact radius (mm)                              |
| $b$   | Stabilization rate for isotropic hardening      |
| $C$   | Coverage (%)                                    |
| $C_l$ | Initial modulus for kinematical hardening (MPa) |
| $D$   | Shot size (diameter) (mm)                       |
| $E$   | Young modulus of the target and the shot (MPa)  |

|                                   |  |
|-----------------------------------|--|
| $\bar{E}$                         | Equivalent Young modulus of the target and the shot (MPa)    |
| $e$                               | Distance between the center of adjacent impacts (mm)         |
| $V$                               | Shot velocity (mm/sec)                                       |
| $\alpha$                          | Impact angle between the shot trajectory and the surface (°) |
| $K$                               | Impact efficiency ratio                                      |
| $k$                               | Number of independent variables                              |
| $n$                               | Number of ranges   |
| $Q$                               | Saturated stress for isotropic hardening (MPa)               |
| $R$                               | Isotropic hardening parameter (MPa)                          |
| $\dot{R}$                         | Rate of isotropic hardening parameter (MPa/sec)              |
| $R^2$                             | Coefficient of determination                                 |
| $R^2_{adj}$                       | Adjusted coefficient of determination                        |
| $r$                               | Strain ratio for cyclic loading                              |
| $\underline{S}$                   | Deviatoric stress tensor (MPa)                               |
| $\underline{X}^{dev}$             | Deviatoric back stress tensor (MPa)                          |
| $\underline{X}$                   | Overall back stress tensor (kinematic hardening) (MPa)       |
| $\underline{X}_l$                 | Kinematic hardening component tensor (MPa)                   |
| $\dot{\underline{X}}_l$           | Rate of kinematic hardening component tensor (MPa/s)         |
| $x_i, x_j$                        | Shot-peening process parameters                              |
| $Y$                               | Yield function (MPa)   |
| $y$                               | Response surface   |
| $Z_{aff}$                         | Affected depth (μm)  |
| $\beta_i, \beta_{ii}, \beta_{ij}$ | Regression coefficients                                      |
| $\epsilon$                        | Second-order model error                                     |
| $\underline{\sigma}$              | Stress tensor (MPa)  |
| $\sigma_{eq}$                     | Equivalent Von Mises stress (MPa)                            |
| $\sigma_{max}$                    | Maximum compressive residual stress (MPa)                    |
| $\sigma_s$                        | Residual stress at the surface (MPa)                         |
| $\sigma_y$                        | Initial yield strength (MPa)                                 |
| $\sigma_0$                        | Yield stress (MPa)   |
| $\underline{\delta}$              | Kronecker delta  |
| $\gamma_l$                        | Nonlinear recovery parameter for kinematical hardening       |

|   |   |
|---|---|
| $\dot{p}$   | Accumulated plastic strain rate ( $s^{-1}$ )  |
| $\Delta\varepsilon_1, \Delta\varepsilon_2, \Delta\varepsilon_3$ | Different applied strain range                |
| $\rho_s$  | Shot density ( $kg/m^3$ )                     |
| $\nu$   | Poisson's ratio                               |
| $a$   | Activation function of the neural network     |
| $b^N$   | Bias of neuron N of the neural network        |
| $\omega_i^N$  | Weights of neuron N of the neural network     |
| $R^2\text{-score}$  | Score of the ANN model                        |
| $\hat{Y}_i$ and $Y_i$   | Predicted data of the ANN model and real data |

## 1. Introduction

Shot-peening is one of the most effective cold working surface treatment processes which is widely employed to enhance the fatigue behavior of many critically loaded mechanical parts in aerospace and automotive industries. During the process, the surface of the mechanical part is impacted by a large number of small particles, called shots made of steel, ceramic, or glass, at a relatively high velocity (up to 100 m/s). As a result, a plastic deformation is induced in the superficial layer. Subsequently, a compressive residual stress field is produced and enhances fatigue life of engineering components [1]. In fact, the presence of compressive residual stresses will impart crack closure stresses, effectively delaying fatigue crack initiation time and reducing the driving force of the crack propagation [2]. Besides, this beneficial effect is generally accompanied by micro cracks, surface roughness, and sometimes microstructural changes. In fact, the use of appropriate shot-peening parameters is highly important. This is because underpeening results in poor induced residual stresses, while overpeening results in serious alteration in surface integrity causing a significant degradation in fatigue strength [3] [4]. Accordingly, the control of the shot-peening parameters has been the subject of many investigations.

A large number of experimental investigations were carried out to study this surface treatment process. These investigations focused on adjusting its influential parameters in order to control its detrimental effects and simultaneously to enhance the beneficial effects arising from the induced compressive residual stresses in a shot peened component [5] [6] [7] [8] [9] [10] [11] [12]. Moreover, this approach was also used to develop empirical models of induced residual stress in terms of process parameters [13] [14]. However, experimental approach is not only

time consuming but requires significant experimental tests for a restricted validation range. This made way for analytical investigations of the process [15] [16] [17] [18]. Analytical models include complex mathematical analyses which are less expensive but they are based on simplifications and assumptions which affect their accuracies when applied to complex geometries. More mechanical methods to predict residual stress profiles from shot-peening parameters are based on the simplified elastoplastic analysis initially proposed by Zarka [19] and applied to conventional shot-peening by Inglebert [20]. It uses the elastoplastic cyclic behavior of the impacted material coupled with the Hertz contact theory. More promising approach for prediction and optimization of shot-peening process is provided by numerical techniques such as the finite element modeling (FEM). It has proven to be highly efficient for better understanding of the peening mechanisms [21]. Consequently, a significant number of research works focused on the use of FEM to analyse the distribution of residual stresses under the effect of shot size [22] [23] [24] [25], shot velocity [22] [23] [25], coverage [26] [27] [28], impact angle [24] [25] [29] [30], and material behavior of the target component [25] [31]. Based on these works, it was shown that the increase in the shot size and the shot velocity results in an increase in the depth of the maximum compressive residual stress as well as the affected depth while the surface and the maximum sub-surface compressive residual stresses are almost not sensitive to these two shot-peening parameters but are mainly related to the mechanical characteristics of the target component material. Increasing the coverage until a certain level shows beneficial effects in terms of all quantities defining the residual stress profile. Finally, a normal impact angle or close to normal impact experiences the most beneficial features of the residual stress field.

TRIP steels have a volume fraction of retained austenite that transforms to martensite during thermomechanical loading. Many experimental studies focused on the deformation-induced martensitic transformation and on the induced work hardening under monotonic loading. As mentioned by [32], the cyclic mechanical response of TRIP steels has barely been investigated by modeling approaches coupling phase transformation and strain cyclic hardening. On a fully metastable austenitic steel, Burgold et al. [32] proposed a cyclic phenomenological model advanced from the approaches developed by [33] or [34] where the phase transformation is triggered after a certain number of cycles induced by the accumulated transformation strain. For different cyclic strain amplitude, the model predicts the stress amplitude directly linked to the strain induced martensitic phase transformation.

Concerning TRIP steels treated by shot-peening, only few studies have investigated the effect of shot-peening including phase transformation in different steel grades. Experimental studies analysed the residual stresses in the different phases such as austenite, ferrite if present, and created martensite, along with their evolving volume fractions [35] [36] [37] [38] [39]. For the modeling of shot-peening with phase transformation, Halilović et al. [40] developed a finite element model for laser shock peening on AISI 304 steel by using a material model developed by [34] and implemented in ABAQUS. Guiheux et al. [38] applied the elastoplastic and phase transformation model developed by Kubler et al. [41] to predict the residual stress fields and phase transformation under a single impact on AISI 301 LN fully austenitic steel. They also considered the model to reproduce the dent microgeometry after impact. The same type of model was applied to the simulation of multiple-impacts on TRIP780 with only 16% of retained austenite that exhibits a martensitic phase transformation during impact. The authors showed that the martensitic transformation has a little beneficial impact on the overall residual stress in the first 50  $\mu\text{m}$ . Martensitic transformation generated more compressive residual stresses ( $\Delta\sigma = 50 \text{ MPa}$ ). Chen et al. [42] modeled a single impact during surface mechanical attrition treatment on a TWIP/TRIP steels. Based on a dislocation density model, they modeled the twinning and transformation kinetics and the resulting mechanical fields under a single impact. Similar to shot-peening, Afzal et al. [43] modeled the residual stress distribution in metastable AISI 301 stainless steel submitted to incremental sheet forming (ISF). Using an Olson and Cohen martensitic transformation kinetics induced by plastic strain with an elastoplastic behavior implemented in ABAQUS, they modeled the radial and tangential stress components and the volume fraction of martensite in a disc after ISF. Despite the different mechanical and microstructural fields are predicted, 3D finite element analysis experiences a high computational cost because of using multiple-impacts model [44].

Machine learning and deep learning techniques can be a good tool to understand features and extrapolate/interpolate data obtained from experimental measurements or from FEM. Artificial neural networks (ANNs) emerged as a new branch of the computation useful for simulations of complex correlation that is difficult to describe with physical models. They are flexible non-linear models used to approximate the outputs of various different processes based on its inputs. ANNs are part of the machine learning branch of artificial intelligence, where one or multiple hidden layers of neural networks are considered. The different steps for building a network are: dataset splitting, architecture, and algorithm. ANN models were used in material processing for machining [45], metal forming and forging [46] [47], additive manufacturing [48], and volume

or surface treatments [49] [50]. Maleki and Farrahi [49] modelled conventional shot-peening of AISI steel via ANNs. They studied the effect of the process parameters (coverage from 100% to 2000% and Almen intensity from 17A to 25A) based on experimental data with 8 configurations. The microhardness, residual stress, and grain size profiles versus depth are analyzed and part of the data from the 8 different profiles were used for training and some of them for testing. They managed to train the ANN to reproduce the missing data with a  $R^2$ -score greater than 0.999. However, no new data with different process parameters were predicted in this study. In another study from [50] on shot-peening of 18CrNiMo-6 steel exhibiting an austenite to martensite phase transformation, an ANN algorithm was used to predict the residual stress profiles in austenite and martensite, the volume fraction of retained austenite, microhardness, and domain size obtained from Cauchy breadth of diffraction peaks. Only 3 different profiles obtained from 3 different sets of process parameters were used. In a same manner, 50% of the data from the profiles were used to train the ANN model and the rest to test the model.

In the field of process optimization, Unal and Maleki [51] proposed a multi-criteria decision making (MCDM) numerical approach applied to shot-peening of Almen strips made of AISI 1070 steel to select the most effective process parameters having an impact on surface roughness and surface hardness. They were able to choose the most effective MCDM technique that eliminates hazardous roughness impact. Li-xing et al. [52] proposed a fuzzy neural network approach (FNN) to model microhardness profiles of TC17 titanium alloy as function of shot-peening parameters. FNN couples ANN with fuzzy set that is suitable to handle noisy and scattered data, which was the case of microhardness in TC17 alloy. The authors were able to reproduce experimental microhardness profiles with a maximum error of 8.5% just below the shot peened surface.

As pointed out, the above-mentioned investigations suffer from some of drawbacks such as time consuming, restricted validation range, simplifications, and high computational cost. Moreover, there have been little approaches dealing simultaneously with several shot-peening parameters potentially influence the residual stresses pattern within the TRIP780 steel. In the present work, a hybrid approach based on response surface methodology (RSM) and ANNs associated with FEM of a shot peened component was developed to build more predictive fast running models. To conduct such a study, a 3D multiple-impacts finite element model was employed to perform several finite element (FE) simulations using central composite design

(CCD) of experiments. Two types of models were then developed: second-order model and feed-forward ANN model using Minitab and Scikit Learn, respectively. The effects of many key parameters on the induced residual stress profile within TRIP780 steel, including the shot diameter, the shot velocity, the coverage, and the impact angle were investigated.

## 2. Methodology for predictive models

### 2.1. Response surface methodology (RSM)

In the present work, several shot-peening simulations are conducted using central composite design (CCD) in order to minimize the simulation work and to build second-order response surface models which provide acceptable accuracy in the resolution of nonlinear responses [53]. The shot-peening-independent parameters used in this study consisted of shot size (D), shot velocity (V), coverage (C), and impact angle ( $\alpha$ ). Each of these parameters were varied over five levels as shown in Table 1 . According to the CCD, a total of 25 simulations were generated including  $2^k$  ( $2^4=16$ ) factor points,  $2 \times k$  ( $2 \times 4=8$ ) star points, and one center point. To maintain rotatability, the upper limit of each variable was coded as  $+2$  ( $\sqrt[4]{16}$ ) and the lower limit as  $-2$ ; these values were used to calculate the shot penning parameters. Table 2 shows the results of 25 simulation parameters forming a central composite design. The shot size (diameter) lies between 0.225 and 0.725 mm, the shot velocity between  $2.5 \times 10^3$  and  $92.5 \times 10^3$  mm/s, the coverage between 25 and 325%, and the impact angle between 22.5 and 90°. It is worth mentioning that the impact angle of 112.5 ° (which is greater than 90 °) is the same as  $\alpha = 67.5^\circ$  and it was used to complete the central composite design matrix.

*Table 1 Shot-peening parameters used in the finite element simulation and their levels.*

| Level | Shot size<br>$D$ (mm) | Shot velocity<br>$V$ ( $\times 10^3$ mm/s) | Coverage<br>$C$ (%) | Impact angle<br>$\alpha$ (°) |
|-------|-----------------------|--|---------------------|------------------------------|
| -2    | 0.225                 | 2.5  | 25                  | 22.5                         |
| -1    | 0.35                  | 25   | 100                 | 45                           |
| 0     | 0.475                 | 47.5                                       | 175                 | 67.5                         |
| 1     | 0.6                   | 70   | 250                 | 90                           |
| 2     | 0.725                 | 92.5                                       | 325                 | 112.5                        |

Table 2 Central composite design matrix for shot-peening simulations.

| Run # | Coded variables     |                           |                   |                              | Actual variables    |  |                   |                              |
|-------|---------------------|---------------------------|-------------------|------------------------------|---------------------|--|-------------------|------------------------------|
|       | Shot size<br>D (mm) | Shot velocity<br>V (mm/s) | Coverage<br>C (%) | Impact angle<br>$\alpha$ (°) | Shot size<br>D (mm) | Shot velocity<br>V ( $\times 10^3$ mm/s) | Coverage<br>C (%) | Impact angle<br>$\alpha$ (°) |
| 1     | 1                   | 1                         | 1                 | 1                            | 0.6                 | 70                                       | 250               | 90                           |
| 2     | 1                   | 1                         | 1                 | -1                           | 0.6                 | 70                                       | 250               | 45                           |
| 3     | 1                   | 1                         | -1                | 1                            | 0.6                 | 70                                       | 100               | 90                           |
| 4     | 1                   | 1                         | -1                | -1                           | 0.6                 | 70                                       | 100               | 45                           |
| 5     | 1                   | -1                        | 1                 | 1                            | 0.6                 | 25                                       | 250               | 90                           |
| 6     | 1                   | -1                        | 1                 | -1                           | 0.6                 | 25                                       | 250               | 45                           |
| 7     | 1                   | -1                        | -1                | 1                            | 0.6                 | 25                                       | 100               | 90                           |
| 8     | 1                   | -1                        | -1                | -1                           | 0.6                 | 25                                       | 100               | 45                           |
| 9     | -1                  | 1                         | 1                 | 1                            | 0.35                | 70                                       | 250               | 90                           |
| 10    | -1                  | 1                         | 1                 | -1                           | 0.35                | 70                                       | 250               | 45                           |
| 11    | -1                  | 1                         | -1                | 1                            | 0.35                | 70                                       | 100               | 90                           |
| 12    | -1                  | 1                         | -1                | -1                           | 0.35                | 70                                       | 100               | 45                           |
| 13    | -1                  | -1                        | 1                 | 1                            | 0.35                | 25                                       | 250               | 90                           |
| 14    | -1                  | -1                        | 1                 | -1                           | 0.35                | 25                                       | 250               | 45                           |
| 15    | -1                  | -1                        | -1                | 1                            | 0.35                | 25                                       | 100               | 90                           |
| 16    | -1                  | -1                        | -1                | -1                           | 0.35                | 25                                       | 100               | 45                           |
| 17    | -2                  | 0                         | 0                 | 0                            | 0.225               | 47.5                                     | 175               | 67.5                         |
| 18    | 2                   | 0                         | 0                 | 0                            | 0.725               | 47.5                                     | 175               | 67.5                         |
| 19    | 0                   | -2                        | 0                 | 0                            | 0.475               | 2.5                                      | 175               | 67.5                         |
| 20    | 0                   | 2                         | 0                 | 0                            | 0.475               | 92.5                                     | 175               | 67.5                         |
| 21    | 0                   | 0                         | -2                | 0                            | 0.475               | 47.5                                     | 25                | 67.5                         |
| 22    | 0                   | 0                         | 2                 | 0                            | 0.475               | 47.5                                     | 325               | 67.5                         |
| 23    | 0                   | 0                         | 0                 | -2                           | 0.475               | 47.5                                     | 175               | 22.5                         |
| 24    | 0                   | 0                         | 0                 | 2                            | 0.475               | 47.5                                     | 175               | 112.5                        |
| 25    | 0                   | 0                         | 0                 | 0                            | 0.475               | 47.5                                     | 175               | 67.5                         |

By using RSM and CCD, a second-order model (Equation (1)) has been developed with 95% confidence level.

$$y = \beta_0 + \sum_{i=1}^k \beta_i x_i + \sum_{i=1}^k \beta_{ii} x_i^2 + \sum_{i < j}^k \beta_{ij} x_i \times x_j + \epsilon \quad (1)$$

where  $y$  is the corresponding response and  $x_i, x_j$  are the  $i^{\text{th}}$  and  $j^{\text{th}}$  variables related to the shot-peening process parameters. The terms  $\beta_i, \beta_{ii}, \beta_{ij}$  are the regression coefficients,  $k$  is the number of independent variables, and  $\epsilon$  is the model error. Accordingly, by using the shot-peening parameters ( $D, V, C, \alpha$ ), Equation (1) could be formulated as follows:

$$\begin{aligned}
y = & \beta_0 + \beta_1 D + \beta_2 V + \beta_3 C + \beta_4 \alpha + \beta_{11} D^2 + \beta_{22} V^2 + \beta_{33} C^2 + \beta_{44} \alpha^2 \\
& + \beta_{12} D \times V + \beta_{13} D \times C + \beta_{14} D \times \alpha + \beta_{23} V \times C + \beta_{24} V \\
& \times \alpha + \beta_{34} C \times \alpha
\end{aligned} \tag{2}$$

It is worth mentioning that the  $\beta$  terms have to be identified using an optimization procedure.

## 2.2. Artificial neural networks (ANNs)

ANNs are arrays of processing based on computational logical structures linked by interconnections. ANNs could be employed to fit any complex and ill-defined database, as mentioned above, and they might be adopted for prediction and optimization purposes [54]. The architecture of a neural network can be described as a directed graph whose nodes correspond to neurons and edges correspond to links between them. As shown in Figure 1, each neuron receives as input a weighted sum of the output neurons which are connected to its incoming edge  $x_i^N$ , such that the output neuron  $Y^{N+1}$  can be formulated as follows:

$$Y^{N+1} = a(b^N + \sum_{0}^{n-1} \omega_i^N \cdot x_i^N) \tag{3}$$

where  $a$  is an activation function,  $b^N$  is the bias and  $\omega_i^N x_i^N$  is the weighted sum of the upstream neurons connected to this one. The bias  $b^N$  and the weights  $\omega_i^N$  of each neuron are determined by the training of the ANN algorithm on part of the data (training data). The choice of the activation function is also critical to optimize the data processing. After training, the coefficient of determination computes the  $R^2$ -score to measure how well the data are likely to be predicted by the model, comparing the predicted data  $\hat{Y}_i$  from the ANN to the real test data  $Y_i$ , for  $n$  samples.

$$R^2 - score = 1 - \frac{\sum_{0}^{n-1} (Y_i - \hat{Y}_i)^2}{\sum_{0}^{n-1} (Y_i - \bar{Y})^2} \tag{4}$$

where  $\bar{Y} = \frac{1}{n} \sum_{0}^{n-1} Y_i$ . A  $R^2$ -score close to 1 is aimed for, in the validation step.

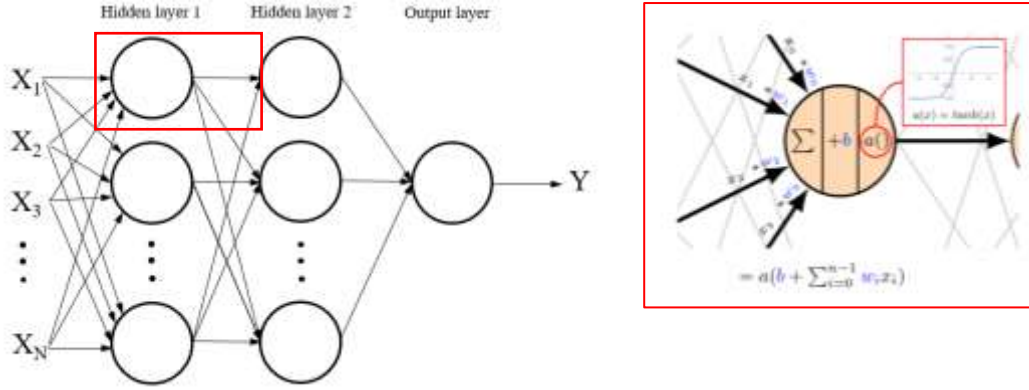


Figure 1 Artificial neural network with two hidden layers. Parameters of the ANN: activation function  $a$ , bias  $b$ .

### 3. Finite element model for multi-impacts shot-peening

#### 3.1. Material constitutive law for TRIP780 steel

Shot-peening can be seen as repetitive impacts of shots on the target material. The Chaboche nonlinear combined isotropic/kinematic hardening model was adopted in this study to represent the cyclic behavior of the target TRIP780 steel [55]. This constitutive law, available in many finite element codes, has been successfully used to predict the flow stress under cyclic loading [56]. In fact, under the effect of multi- impacts, the superficial layer material encounters repeated impacts and hence cyclic loading occurs [57] [58]. In this model, the yield function  $Y$ , defining the yield surface, is expressed as follows:

$$Y = \sigma_{eq} - \sigma_y - R \quad (5)$$

where  $\sigma_y$  is the initial yield strength,  $R$  is the isotropic hardening parameter defined in Equation (10), and  $\sigma_{eq}$  is the equivalent Von Mises stress defined as:

$$\sigma_{eq} = \sqrt{\frac{3}{2}(\underline{S} - \underline{X}^{dev}) : (\underline{S} - \underline{X}^{dev})} \quad (6)$$

where  $\underline{S}$  is the deviatoric stress tensor and  $\underline{X}^{dev}$  is the deviatoric back stress tensor and can be expressed as follows:

$$\underline{X}^{dev} = \underline{X} - \frac{1}{3} tr(\underline{X}) \underline{\delta} \quad (7)$$

where  $\underline{\delta}$  is Kronecker delta and  $\underline{X}$  is the overall back stress (kinematic hardening) which is a combination of several kinematic hardening components  $\underline{X}_l$ , additively decomposed such as:

$$\underline{X} = \sum_{l=1} \underline{X}_l \quad (8)$$

where the rate of  $\underline{X}_l$  is expressed by the nonlinear Ziegler-Prager model implemented in ABAQUS [59] [60]:

$$\dot{\underline{X}}_l = C_l \frac{(\underline{\sigma} - \underline{X})}{\sigma_0} \dot{p} - \gamma_l \underline{X}_l \dot{p} \quad (9)$$

where  $C_l$  is the initial hardening modulus,  $\sigma_0$  the yield stress depending on the isotropic hardening,  $\gamma_l$  is the nonlinear recovery parameter, and  $\dot{p}$  is the accumulated plastic strain rate.

The isotropic hardening parameter  $R$  is defined in its rate form by:

$$\dot{R} = b (Q - R) \dot{p} \quad (10)$$

where  $b$  and  $Q$  are the stabilization rate and the saturated stress of  $R$ , respectively.

In this work two sets of kinematic hardening parameters ( $C_1, \gamma_1, C_2, \gamma_2$ ) and one set of isotropic hardening parameters ( $b, Q$ ) are considered as material constants and they are determined based on experimental approach. In this approach, tensile and cyclic uniaxial tests were used to characterize and assess the performance of the proposed constitutive law model. All tests were performed at room temperature under total strain-controlled loading and in quasi-static strain-rate conditions ( $\dot{\epsilon} = 1 \times 10^{-3} \text{ s}^{-1}$ ). Three different tests are used for material constants characterization: one tensile test and two different incremental cyclic tests performed at strains ratio of -1 and 0, respectively. The specimens used in the testing were extracted from nominal

2 mm thick metal sheets, oriented along the sheet transverse direction ( $90^\circ$  to rolling direction). The characterization procedure is divided into three steps using the Z-set object oriented finite element software [61]. Firstly, the initial yield stress ( $\sigma_y$ ) and the first set of kinematic hardening parameters ( $C_1, \gamma_1$ ) were identified based on the tensile stress-strain curve. Secondly, the isotropic hardening parameters ( $b, Q$ ) and the second set of kinematic hardening parameters ( $C_2, \gamma_2$ ) were identified based on the tensile test and the incremental cyclic test ( $r = -1$ ) and by using the value of ( $\sigma_y, C_1, \gamma_1$ ) obtained from the first step. Finally, the last characterization was conducted on all material constants using the tensile test and the two cyclic tests. Table 3 shows the identified material constants for TRIP780 steel grade.

*Table 3 Material parameters of the constitutive behavior with Chaboche nonlinear combined isotropic/kinematic hardening model for TRIP780 steel grade*

|   |
|---|
| Kinematic hardening parameters:<br>$C_1 = 4495$ (MPa), $\gamma_1 = 9$ (-), $C_2 = 15 \times 10^4$ (MPa), $\gamma_2 = 500$ (-) |
| Isotropic hardening parameters:<br>$b = 500$ (-), $Q = -200$ (MPa), $\sigma_y = 475$ (MPa)                                    |

An additional experimental test was carried out to validate the model prediction capability for loading conditions that are close to those encountered in the superficial layer material under the effect of multi-impacts. This test consists of an initial monotonic loading until a total strain of 2.5% followed by an incremental cyclic loading up to 50 cycles at different strain ranges ( $\Delta\epsilon_1 = 0.7\%$ ,  $\Delta\epsilon_2 = 1.5\%$ , and  $\Delta\epsilon_3 = 2.4\%$ ). This test is simulated through a 2D finite element simulation using ABAQUS software [62]. In this simulation the sample, modeled as an elasto-plastic body (1 mm long  $\times$  1 mm high), was meshed by means of 1 continuum, plane stress, CPS4R element. Referring to the boundary conditions, the loading conditions are the same as those used in the experimental test. The normal translations were restrained on the left and the bottom faces in X and Y directions, respectively. Figure 2 shows the comparison between experimental and the predicted cyclic behavior for TRIP780 steel. Though the predicted true stress-strain hysteresis loops do not match exactly with the measured ones, it appears that an overall good prediction is obtained.

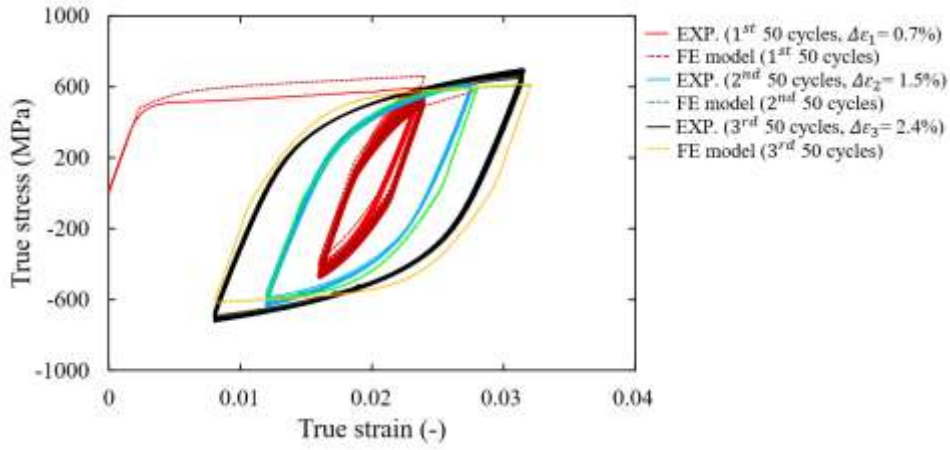


Figure 2 Incremental cyclic strain-controlled tensile tests (mean strain = 2.5%): comparison between experimental (EXP.) and predicted (FE model).

### 3.2. Finite element model and parameters

A 3D finite element model was used to simulate the shot-peening process of TRIP780 steel, using the commercial finite element software ABAQUS [62]. An explicit integration method was employed to take into account the shot-peening dynamic effects. In this simulation, a Python script was developed to automate the model generation with particular inputs related to shot-peening conditions, numerical aspects, boundary conditions, and contact properties.

The simulations of multi-impacts in the current work were carried out using a model consisting of 37 shots impacting the target component, considered as a semi-infinite medium (i.e., it is sufficiently massive to limit its global deformation), with a predetermined way (hexagonal pattern) where the distance between the center of adjacent impacts of radius “a” is equal to “e”, as given schematically in Figure 3 (a). It is worth mentioning that the model has one symmetry plane (X-Z plane) for enhancing the computational efficiency; therefore, a total of 22 shots arranged in four ranges (n=4) were only modeled including 7 half-shots and 15 whole shots situated in the plane of symmetry and behind it, respectively (see Figure 3 (a)). It is worth mentioning that for a given simulation from Table 2, the size of all the shots is constant. The velocity magnitude of the shots is also constant and is set just before the impact so that the shots have a free flight and the interaction between the shots and the surface is then calculated. The angle  $\alpha$ , that changes the velocity vector direction, is set in planes parallel to the X-Z plane and corresponds to the angle between the surface and the shot trajectory before the impact. A 90° impact angle is an impact of shots normal to the surface. In fact, previous work [63] showed that a variability of shot diameters does not affect the residual stress profile. A variability of

impact velocities does not affect the surface stress nor the maximal compressive stress. It only has a slight effect on the affected depth.

The target component was modeled as having different regions in order to provide a dense mesh in the zone of interest (impact zone); two rectangular regions in the X-Y plane and two layers stacked in the depth direction (Z-direction). The dimensions of each region are parameterized based on the impact radius “a”, the distance between the center of adjacent impacts “e”, and the number of ranges “n” as depicted in Figure 3 (b). These dimensions are determined from convergence study such that the predicted results are not sensitive to the applied boundary conditions far from the impact zone.

The impact radius  $a$  of a single shot is estimated based on Hertz theory as follows [64] [65]:

$$a = D \left( \frac{K \pi \rho_s V^2}{4 \sqrt{2} \bar{E}} \right)^{1/5} \quad (11)$$

where  $D$  is the shot size;  $K$  is the impact efficiency ratio;  $\rho_s$  is the shot density;  $V$  is the shot velocity; and  $\bar{E}$  is the equivalent Young modulus of the target and the shot.

The impact efficiency ratio  $K$  is characterized by the ratio between the elasto-plastic energy and the total kinetic energy. A value of 0.8 was used in this work according to [66].

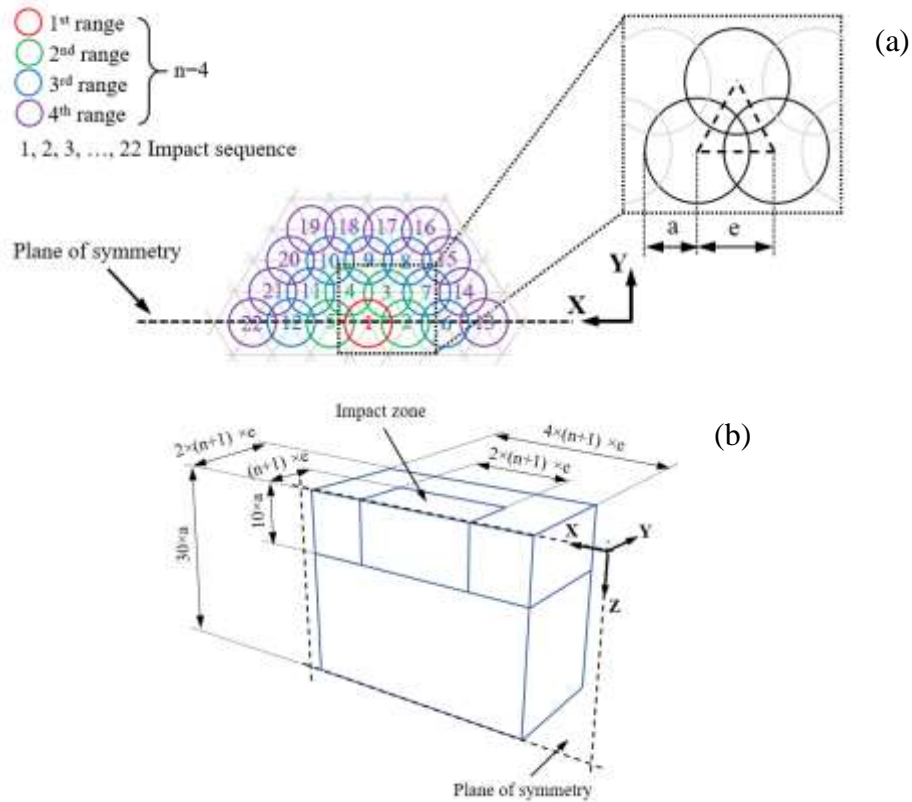
The distance between the center of adjacent impacts “e” can be given with respect to the impact radius  $a$  and the coverage rate “C” by [67]:

$$e = 10 a \sqrt{\frac{2 \pi}{\sqrt{3} C}} \quad (12)$$

Overlaps between shot impacts are implicitly taken into account when the impact radius “a” is greater than the distance between the impacts “e”, therefore increasing the coverage “C”.

The shot was considered as an elastic body meshed using C3D8R elements. The target component, modeled as an elasto-plastic body, consists of two element types: C3D8R elements

in the impact zone and C3D4 elements for the rest of target. In order to carry out different shot-peening conditions, it was chosen to use an element size as a function of the distance between the center of adjacent impacts “ $e$ ”. Thereby, the element size is found to be within [0.01-0.09 mm] and [0.003-0.025 mm] for the shots and target top surface in the impact zone, respectively. Additionally, a biased meshing scheme was adopted along the impact zone depth in order to keep a dense mesh underneath the impacted surface and a coarse one at the bottom. This appropriate meshing size is determined from convergence mesh simulations such that the predicted results are not sensitive to these inputs. Figure 3 (c) shows the adopted mesh. As mentioned before (section 3.1.), the Chaboche constitutive law was utilized to represent the elasto-plastic behavior of the target material. The elastic material properties for both shot and target component are: Young’s modulus  $E = 210$  (GPa), the Poisson’s ratio  $\nu = 0.3$ , and the density  $\rho_s = 7800$  (kg/m<sup>3</sup>). It is worth mentioning that the strain sensitivity effect is moderate for TRIP780 steels [68], thus the strain-rate effect was not considered in the model.



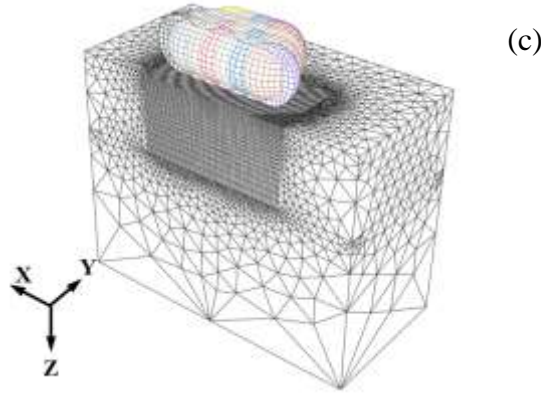


*Figure 3 FE model: (a) hexagonal impact pattern and the impact sequence for  $n$  ranges. Impact radius  $a$ , distance between impacts  $e$ , (b) geometry of the target part with the impact zone, (c) mesh of the shots (C3D8R) and the target (C3D8R in the impact zone and C3D4 elements in the surrounding).*

Symmetry boundary conditions were applied on the shots located in the plane of symmetry and one lateral surface of the target. The translations of the faces of the target were restrained along their normal directions, except the top face. The shots were initially kept very near to the target body, at a distance of 0.1 mm, to reduce the time of bringing them into contact and hence enhancing the computational efficiency, and then propelled towards the stationary target at a velocity magnitude  $V$  exerted on all nodes of shots and in the X-Z plane. Penalty algorithms coupled to normal and tangential behaviors with isotropic Coulomb friction coefficient of 0.4 were employed between shots (master surface) and the target surface (slave surface).

A damping time was added to the model with time duration sufficient to allow the damping of the target component and consequently to avoid the residual stress oscillations.

## 4. Results and discussion

### 4.1. Finite element modeling

#### 4.1.1. Validation of the shot-peening model for TRIP780 steel

The first step in the current investigation was to prove the validity of the proposed finite element shot-peening model. This was carried out by comparing the predicted residual stress profiles ( $\sigma_{11} - \sigma_{33}$ ) in one direction (X in-plane direction according to Figure 3 (c)) within TRIP780 steel to its corresponding experimental profiles [39] obtained by XRD technique and under similar shot-peening (SP) conditions: (1)  $D = 0.4$  (mm),  $V = 60 \times 10^3$  (mm/s),  $C = 230$  (%),  $\alpha = 90$

(°) and (2)  $D= 0.6$  (mm),  $V= 60 \times 10^3$  (mm/s),  $C= 270$  (%),  $\alpha= 90$  (°). All the presented FE results were extracted using a post-processing script based on taking the average at nodes, at each depth with respect to the undeformed mesh, situated in an hexagonal zone corresponding to the 4<sup>th</sup> range of the target component (hexagon of radius of  $3 \times e$ ) as depicted in Figure 4. This was done in order to avoid the impact sequence effects. Figure 5 shows the predicted and experimental results. It is clear that the predicted and measured residual stress profiles are well correlated. The maximal residual stress is only slightly affected by the diameter increase. The affected depth increases with the diameter from 300  $\mu\text{m}$  to 500  $\mu\text{m}$ . This affected depth is slightly overestimated by the FE model for SP conditions no. 1 being closer to 270  $\mu\text{m}$ . A comparison of the present material model response can be made with another model that includes phase transformation. The affected depth with this model is similar to the model with phase transformation presented in [39] (300  $\mu\text{m}$  for SP conditions no. 1 and close to 500  $\mu\text{m}$  for SP conditions no. 2). Kubler et al. [39] also showed that only the first 100  $\mu\text{m}$  (resp. 200  $\mu\text{m}$ ) is affected by martensitic phase transformation for SP conditions no. 1 (resp. SP conditions no. 2). They predicted that 4 to 6% of the retained austenite (initially 13%) is still present in the first 50-100  $\mu\text{m}$ . It appears that the predicted profiles give the same trends and the same type of residual stress level at surface as the measured ones. It is also important to bear in mind that a good correlation between the predicted and experimental results is difficult to obtain. The differences can be correlated to different sources. The experimental measurement of the residual stresses, the thickness of the etched layer, and the material homogeneity are to name a few. Additionally, the material behavior modeling, friction conditions, numerical integration, and discretization are error sources attributed to FEM. Based on the above comparisons, the developed shot-peening model can be used to conduct several simulations based on CCD (Table 2) to develop second-order and ANN models for residual stresses as pointed out in next sections.

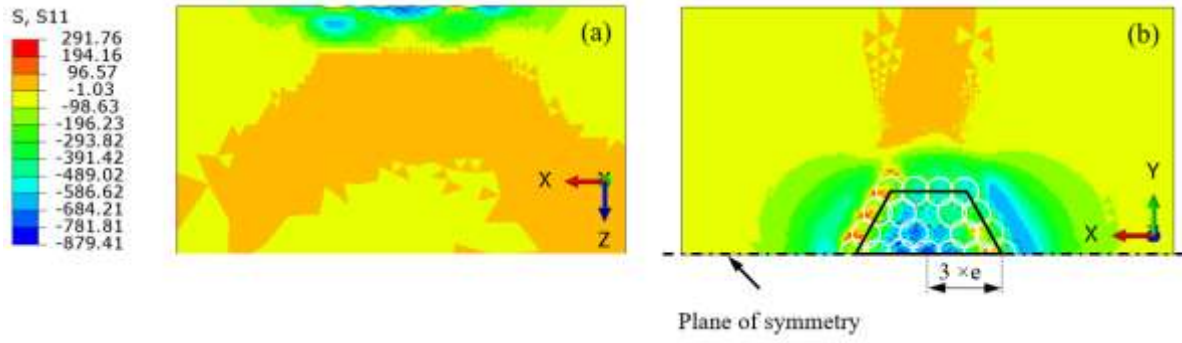


Figure 4 FE results: residual stress ( $S_{xx}$  in MPa) after impact at the target surface. The initial positions of the shots and the averaging zone of size  $3 \times e$  are shown: (a) front view (b) top view.

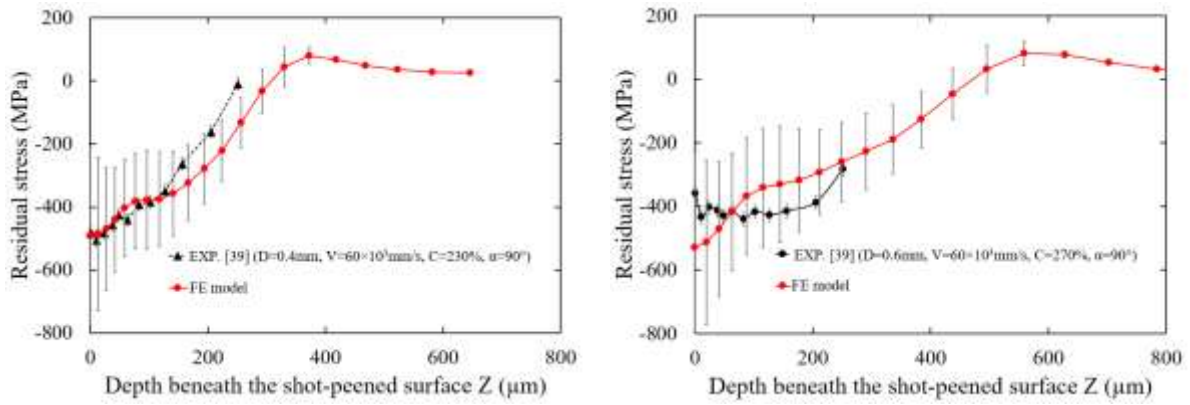
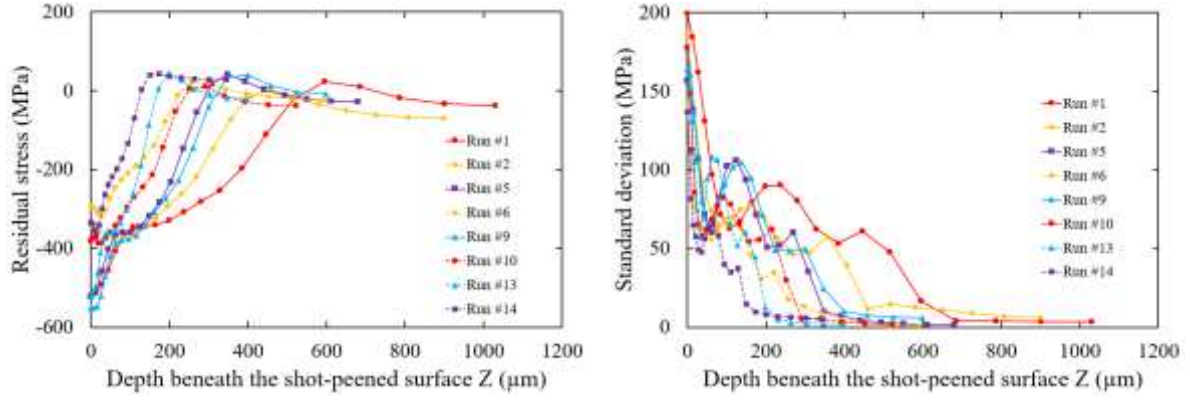


Figure 5 Residual stress profiles ( $S_{xx}$ ) for TRIP780 steel after shot-peening with two conditions: comparison between experimental data (EXP.) and simulations (FE model). The error bars represent the error in measuring the residual stresses for the experimental profile, while they represent the standard deviation in the averaged nodes situated in the hexagonal zone for the FE profile.

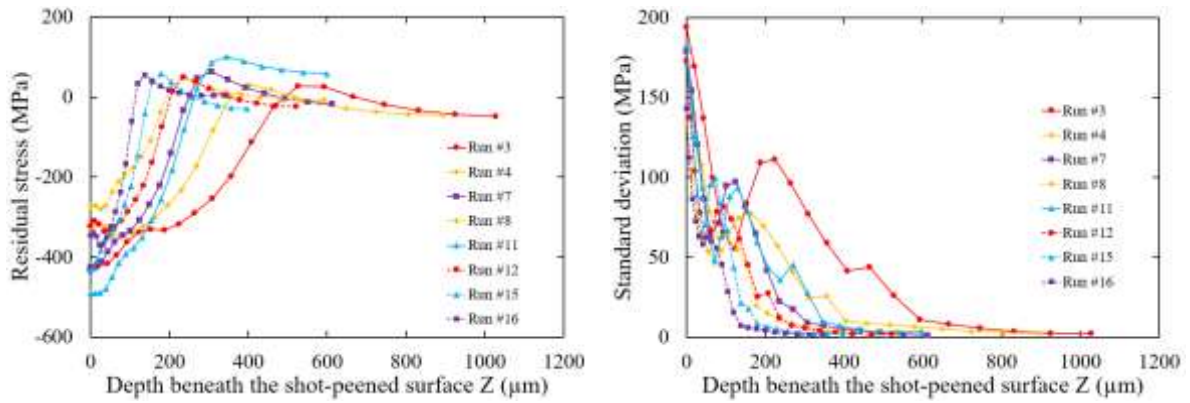
#### 4.1.2. Residual stress profiles

The different averaged profiles of stresses are output along the depth ( $Z$ ) from the different FE simulations. Figure 6 shows the residual stress profiles of several FE simulations carried out based on the CCD (Table 2) and their standard deviation profiles. For the sake of clarity, these results are presented in 3 charts in Figure 6. Figure 6 (a) and Figure 6 (b) show respectively the residual stress profiles for coverage rates of 250% and 100%. The effect on residual stress profiles of coverage rates of 25%, 175% and 325% are presented in Figure 6 (c). It is clear that the process parameters have an effect on the quantities defining the residual stress profile (reduced parameters) such as the residual stress at the surface ( $\sigma_s$ ), the maximum compressive

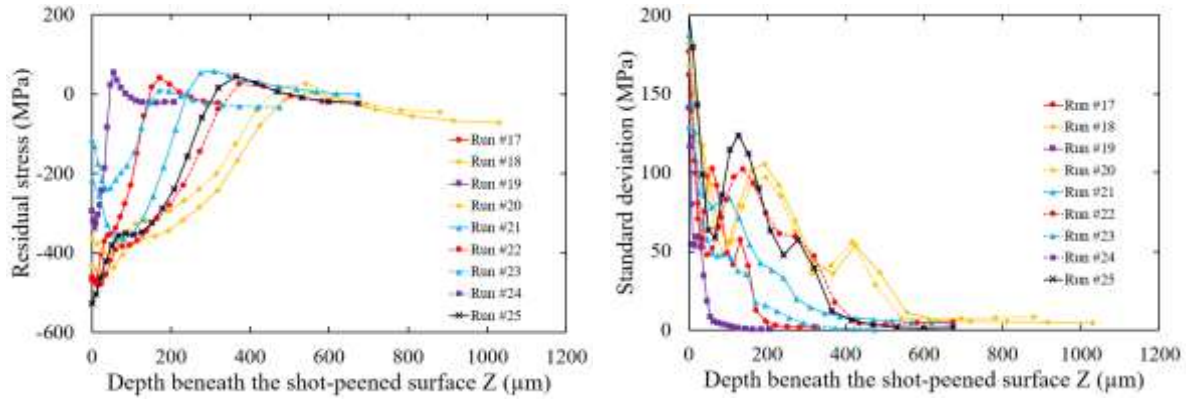
residual stress ( $\sigma_{max}$ ), and the affected depth ( $Z_{aff}$ ) where the residual stress comes back to a positive value. With increasing the shot size, the shot velocity, and the impact angle, the residual stress at the surface also increased. Results show that the increase in the shot size, the shot velocity, and the coverage results in an increase in the affected depth. Increasing the shot velocity and the coverage shows an increase in the maximum compressive residual stress. While this latter is only slightly affected when increasing shot size. Changing the impact angle from  $22.5^\circ$  to  $90^\circ$  (normal impact =  $90^\circ$ ) results in an increase in the affected depth as well as the maximum compressive residual stress. Moreover, an impact angle  $\alpha$  of  $90^\circ$  leads to a maximum stress at the surface, and for angles less than  $90^\circ$ , the maximal compressive residual stress is shifted from the surface to a depth of 20-80  $\mu\text{m}$ . These results are in good agreement with the previous works [25] [26] [29] and could be explained by the fact that more energy is transferred to deform the deeper layer due to Hertzian loads [5]. As can be seen in Figure 6, larger standard deviations (up to 200 MPa for a residual stress of  $-400$  MPa) were obtained at the shot peened surface and decrease along the depth. This is because the severe boundary conditions (shots-impact zone contact) are more pronounced at surface and sub-surface which result in inhomogeneous mechanical fields.



(a) Profiles with a coverage rate of 250%



(b) Profiles with a coverage rate of 100%



(c) Profiles with other coverage rates (25%, 175% and 325%)

Figure 6 FE simulation: residual stress profiles ( $S_{xx}$ ) and their standard deviation profiles for the different runs defined by the central composite design matrix (Table 2).

#### 4.2. Prediction with second-order models

In this section, second-order models for in-depth residual stresses as well as their reduced parameters were developed based on FEM results shown in Figure 6. These models are given

in terms of the shot-peening-independent parameters: shot size (D), shot velocity (V), coverage (C), and impact angle ( $\alpha$ ). A stepwise regression procedure was adopted to identify significant terms of the response (i.e., when P value < 5%), [53]. The final regression coefficients determined by Minitab software to build the mathematical models for TRIP780 steel are given in Table 4 and Table 5. The coefficient of determination  $R^2$ , the adjusted coefficient of determination  $R_{adj}^2$ , and the P value are also presented in these tables. Referring to in-depth residual stresses, the coefficient of determination  $R^2$  and the adjusted coefficient of determination  $R_{adj}^2$ , for the response values at depth ranging from 0 to 320 $\mu$ m, are found to be within [79.81-95.81%] and [74.5-93.71%], respectively, while these coefficients decrease for the rest of depth. As far as the reduced parameters, the coefficient of determination  $R^2$ , for all quantities, is found to be within [80.45-95.61%] while the adjusted coefficient of determination  $R_{adj}^2$ , is found to be within [77.66-94.14%]. These results indicate that the second-order polynomial model gives an overall good prediction of the induced residual stresses. In order to validate the developed models, four extra shot-peening simulations were performed as listed in Table 6. Figure 7 shows that the predicted in-depth residual stresses using mathematical models and FEM are well correlated. Regarding the reduced parameters, it can be seen from Figure 8 that the predicted values using the mathematical models are within 23%, 4.3%, and 15.4% of numerical predicted values for the residual stress at the surface ( $\sigma_s$ ), the maximum compressive residual stress ( $\sigma_{max}$ ), and the affected depth ( $Z_{aff}$ ), respectively. Based on the above analysis, the developed mathematical models can be used to investigate different shot-peening conditions within fixed ranges of shot-peening-independent parameters.

Table 4 Model parameters for the second-order model (Equation (2)) predicting in-depth residual stress profiles.

| Residual stress ( $\sigma_{11} - \sigma_{33}$ ) (MPa) |                         |        |        |        |          |              |              |              |                        |              |                   |   |       |             |
|---|-------------------------|--------|--------|--------|----------|--------------|--------------|--------------|------------------------|--------------|-------------------|---|-------|-------------|
| Depth<br>( $\mu\text{m}$ )                            | Regression coefficients |        |        |        |          |              |              |              |                        |              |                   | P value                                   | $R^2$ | $R^2_{adj}$ |
|   | $Const.$                | $D$    | $V$    | $C$    | $\alpha$ | $D \times D$ | $V \times V$ | $C \times C$ | $\alpha \times \alpha$ | $D \times V$ | $V \times \alpha$ |   |       |             |
| 0   | -372.7                  | -      | -      | -38.3  | -87.2    | -23.8        | -            | -            | -                      | -            | -                 | 0.002 ; 0 ; 0.032                         | 80.45 | 77.66       |
| 5   | -373.8                  | -      | -      | -39.16 | -86.65   | -23.09       | -            | -            | -                      | -            | -                 | 0.001 ; 0 ; 0.026                         | 82.65 | 80.17       |
| 10  | -374.2                  | -      | -      | -39.36 | -81.66   | -22.94       | -            | -            | -                      | -            | -                 | 0 ; 0 ; 0.019                             | 83.22 | 80.82       |
| 20  | -373.5                  | -      | -19.87 | -33.55 | -65.9    | -18.51       | -            | -            | -                      | -            | -                 | 0.03 ; 0.001 ; 0 ; 0.038                  | 81.21 | 77.45       |
| 30  | -419.4                  | -      | -33.29 | -21.6  | -53.19   | -            | 25.01        | -            | 17.54                  | -            | -                 | 0.001 ; 0.015 ; 0 ; 0.007 ; 0.047         | 80.44 | 75.29       |
| 40  | -394.1                  | -      | -50.05 | -      | -45.76   | -            | 35.01        | -            | -                      | -            | -                 | 0 ; 0 ; 0.002                             | 74.25 | 70.57       |
| 50  | -387.9                  | -      | -61.7  | -      | -42.2    | -            | 46.9         | -            | -                      | -            | -                 | 0 ; 0.001 ; 0                             | 75.25 | 71.72       |
| 75  | -379.6                  | -      | -61.13 | -      | -41.39   | -            | 47.09        | -            | 22.04                  | -            | -                 | 0 ; 0 ; 0 ; 0.021                         | 83.76 | 80.51       |
| 100   | -371.2                  | -31.82 | -66.14 | -      | -49.88   | 16.16        | 48.37        | -            | 26.85                  | 17.6         | 26.62             | 0 ; 0 ; 0 ; 0.015 ; 0 ; 0 ; 0.016 ; 0.001 | 95.81 | 93.71       |
| 130   | -209.1                  | -64    | -82.4  | -      | -59.1    | -            | -            | -27.7        | -                      | 37.3         | -                 | 0 ; 0 ; 0 ; 0.018 ; 0.011                 | 87.75 | 84.53       |
| 170   | -180.2                  | -85    | -90.1  | -      | -54.5    | -            | -            | -            | -                      | -            | -                 | 0 ; 0 ; 0.001                             | 82.76 | 80.29       |
| 200   | -144.4                  | -80.5  | -85    | -25,3  | -55.1    | -            | -            | -            | -                      | -            | -                 | 0 ; 0 ; 0.047 ; 0                         | 85.87 | 83.05       |
| 240   | -99                     | -68.4  | -73.6  | -31,4  | -40.6    | -            | -            | -            | -                      | -43.6        | -                 | 0 ; 0 ; 0.007 ; 0.001 ; 0.003             | 87.15 | 83.77       |
| 280   | -62.2                   | -57.3  | -60    | -26,9  | -        | -            | -            | -            | -                      | -60.3        | -                 | 0 ; 0 ; 0.024 ; 0                         | 80.6  | 76.72       |
| 320   | 20.4                    | -46.4  | -43.9  | -      | -        | -32.9        | -26.7        | -            | -                      | -57.3        | -                 | 0 ; 0 ; 0.005 ; 0.018 ; 0                 | 79.81 | 74.5        |
| 380   | -16.3                   | -27.3  | -      | -      | -        | -            | -            | -            | -                      | -34.9        | -                 | 0.035 ; 0.028                             | 32.48 | 26.34       |
| 520   | -5.18                   | -      | -      | -      | -        | -            | -            | -            | -                      | -            | 14.2              | 0.01                                      | 25.69 | 22.46       |
| 600   | -9.54                   | -      | -      | -      | -        | -            | -            | -            | -                      | -            | 19.61             | 0   | 47.81 | 45.54       |
| 800   | -19.85                  | -11.51 | -      | -      | -        | -            | -            | -            | -                      | -            | 17.02             | 0 ; 0.001                                 | 52.2  | 47.85       |
| 1000  | -22.42                  | -14.65 | -      | -      | -        | -            | -            | -            | -                      | -            | 15.1              | 0.002 ; 0.007                             | 49.29 | 44.68       |

Table 5 Model parameters for the second-order model (Equation (2)) predicting reduced parameters of the residual stress profile ( $\sigma_s$ ,  $\sigma_{max}$ ,  $Z_{aff}$ ).

| Source                 | $\sigma_s$ (MPa)        |         | $\sigma_{max}$ (MPa)    |         | $Z_{aff}$ (mm)          |         |
|------------------------|-------------------------|---------|-------------------------|---------|-------------------------|---------|
|                        | Regression coefficients | P Value | Regression coefficients | P Value | Regression coefficients | P Value |
| Constant               | -372.7                  | -       | -473.6                  | -       | 0.26444                 | -       |
| $D$                    | -                       | -       | 11.18                   | 0.017   | 0.08169                 | 0       |
| $V$                    | -                       | -       | -13.43                  | 0.005   | 0.09378                 | 0       |
| $C$                    | -38.3                   | 0.002   | -28.32                  | 0       | 0.023                   | 0.003   |
| $\alpha$               | -87.2                   | 0       | -70.48                  | 0       | 0.03375                 | 0       |
| $D \times D$           | -23.8                   | 0.032   | -                       | -       | 0.01865                 | 0.011   |
| $V \times V$           | -                       | -       | 25.36                   | 0       | -                       | -       |
| $C \times C$           | -                       | -       | 11.48                   | 0.025   | -                       | -       |
| $\alpha \times \alpha$ | -                       | -       | 21.83                   | 0       | -                       | -       |
| $D \times V$           | -                       | -       | -                       | -       | 0.02144                 | 0.018   |
| $C \times \alpha$      | -                       | -       | -13.94                  | 0.015   | -                       | -       |
| $R^2$                  | 80.45%                  | -       | 96.08%                  | -       | 95.61%                  | -       |
| $R^2_{adj}$            | 77.66%                  | -       | 94.11%                  | -       | 94.14%                  | -       |

Table 6 Additional shot-peening parameters used in FE simulation for validation purpose.

| Run # | Actual variables    |  |                   |                                 |
|-------|---------------------|--|-------------------|---------------------------------|
|       | Shot size<br>D (mm) | Shot velocity<br>V ( $\times 10^3$ mm/sec) | Coverage<br>C (%) | Impact angle<br>$\alpha$ (deg.) |
| 26    | 0.3                 | 80   | 210               | 55                              |
| 27    | 0.4                 | 15   | 290               | 80                              |
| 28    | 0.55                | 35   | 60                | 100                             |
| 29    | 0.65                | 60   | 150               | 40                              |

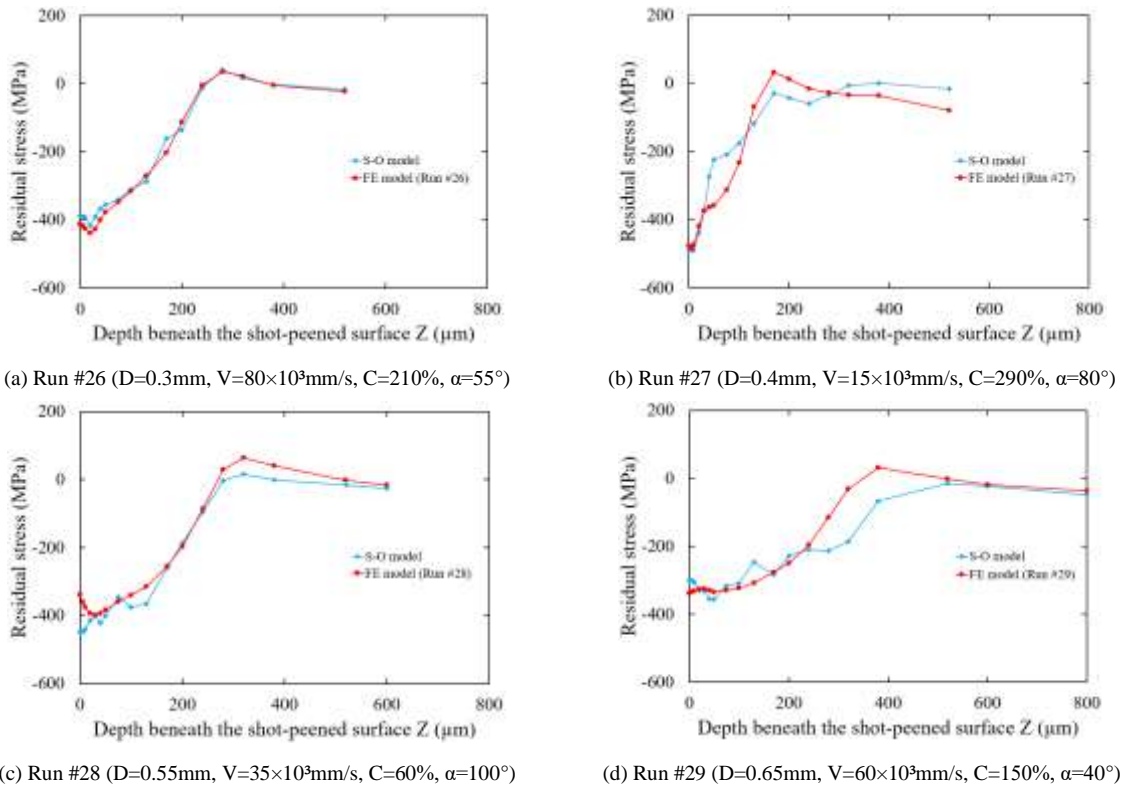


Figure 7 Comparison between the second-order model prediction (S-O model) and the finite element one (FE model) of residual stress profiles ( $S_{xx}$ ).

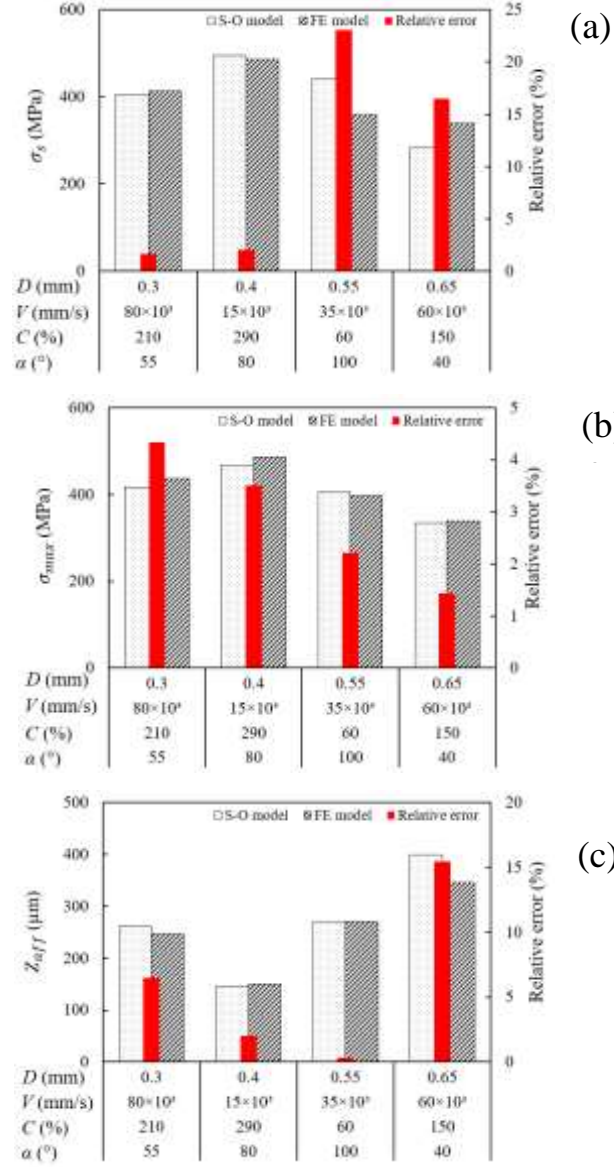


Figure 8 Comparison between the second-order model prediction (S-O model) and the finite element one (FE model) of: (a) residual stress at the surface  $\sigma_s$ , (b) maximum compressive residual stress  $\sigma_{max}$ , and (c) affected depth  $Z_{aff}$ .

### 4.3. Prediction with the ANN model

#### 4.3.1. Neural network and sensitivity analysis

In this work, the SciKit learn software for Python [69] was used with the Multi-Layer Perceptron technique (MLP). MLP is a class of feedforward artificial neural network that is suitable for tabular data analysis, despite there are no recurrent connections, no parameter sharing, no spatial relationship compared to recurrent neural network (RNN) or convolutional neural network (CNN).

The tabular dataset obtained by FE analysis (Figure 6) for different process parameters is provided to the MLP. A total of 591 data sets were used. Those data sets consist of the residual stress data points at a given depth ( $Z$ ) for a set of process parameters ( $C, V, D, \alpha$ ). The inputs of the ANN model are the process parameters and the depth ( $Z$ ), and the output is the residual stress ( $\sigma_{11} - \sigma_{33}$ ). A regression is performed based on the optimization of the loss function (square error). The gradients of the loss function with respect to each weight were calculated using the “Adam” solver [70]. “Adam” solver refers to a stochastic gradient-based optimizer which is advised for relatively large datasets and works well in terms of training and validation score. A single hidden layer is used. The effect of the number of neurons was investigated by varying the training from 20 to 50 neurons. For nonlinear problems, the *tanh* activation function gave better preliminary results in terms of validation score. The other parameters are L2 penalty parameter for regularization: 0.0001 and the tolerance for optimization which was set to  $10^{-6}$  for 1000 epochs.

The ANN model was trained 3 times with 85% of the data randomly extracted from the FE simulations and 15% of the data were used to calculate the score obtained by the ANN model. The best  $R^2$ -score out of the three attempts was kept as the prediction model. Before training, input data were normalized so that the shot size lies between 0.1 and 1 mm, the shot velocity between 1 and  $100 \times 10^3$  mm/s, the coverage between 10 and 500 %, and the impact angle between  $0^\circ$  and  $90^\circ$ . The depth at which the residual stress was obtained, is also an input of the ANN model. Depths were normalized between 0 and 2 mm. This scaling step prevents one input variable to dominate all others by having much larger values and variances.

Figure 9 shows the results of the trained ANN model on the training FE data set for different number of neurons. Results show that 20 neurons are not enough to reproduce the residual stress profiles. Besides, a high number of neurons could lead to overfitting of the data. Preliminary simulations showed that from 20 neurons the  $R^2$ -score is close to 0.99. Those are the reasons why a model with 25 neurons was selected.

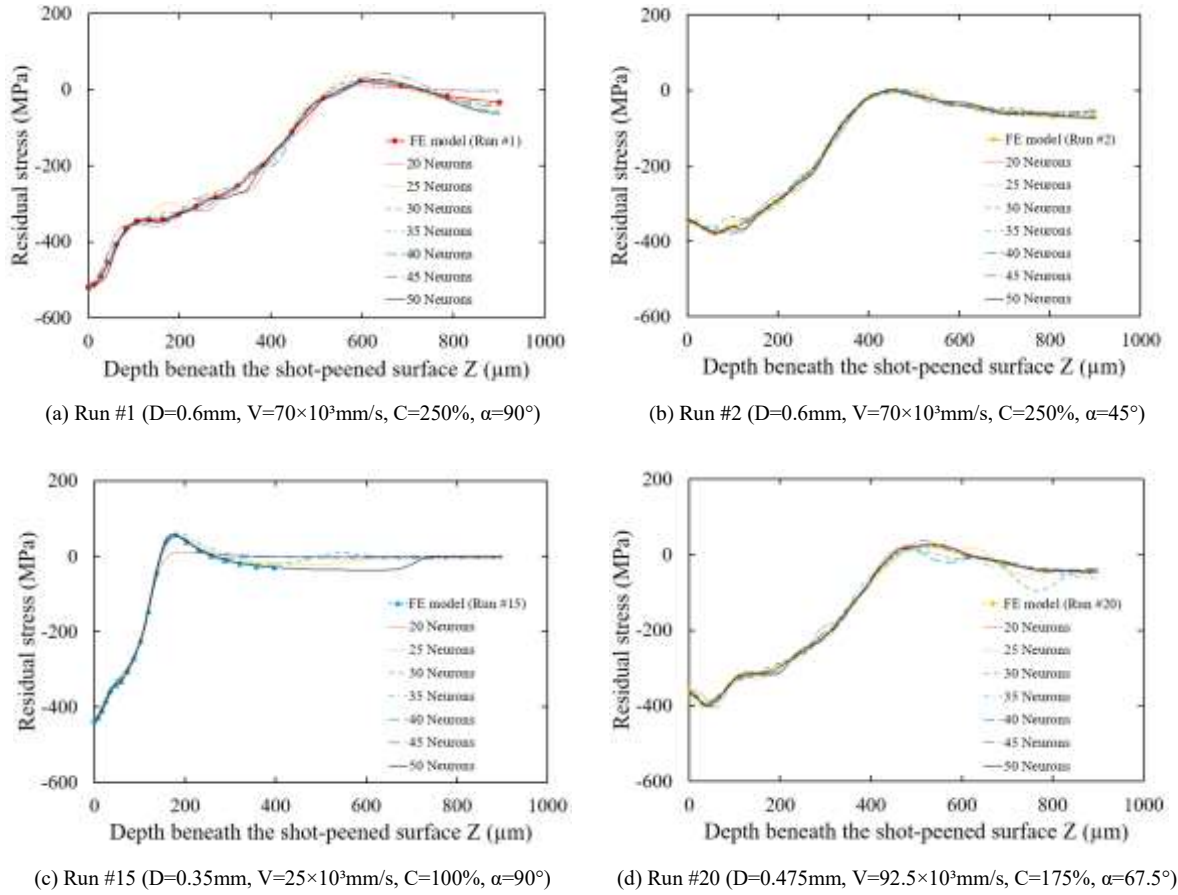
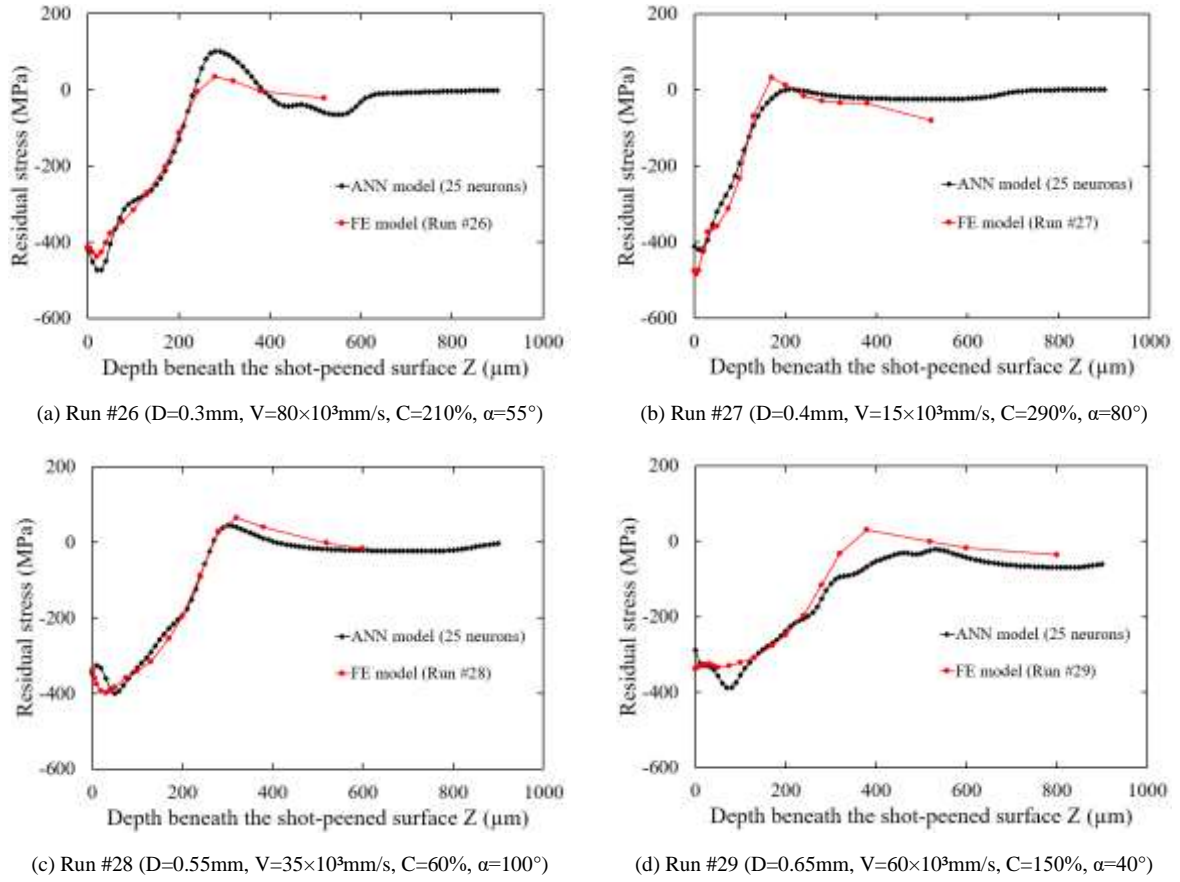


Figure 9 Residual stress profiles obtained with the ANN model after training – effect of the number of neurons for different sets of process parameters. Comparison with FE model.

#### 4.3.2. ANN model

The residual stresses predicted by ANN model were first compared to those obtained by FEM based on the shot-peening conditions listed in Table 6. The ANN model was then used to analyze the effect of each shot-peening parameter on the output response.

Figure 10 shows the prediction of the ANN model with 25 neurons and 1 hidden layer. It appears that the ANN model with 25 neurons comparatively predicts well the shape of the residual stress profile as well as the maximal compressive stress and its location beneath the surface. The evolution of the affected depth is also well reproduced except for Run #29 (Figure 10 (d)). This is because the impact angle of  $40^\circ$  was used for this run which is slightly out the training range of  $45^\circ$ - $90^\circ$ .



*Figure 10 Comparison between the ANN model and the finite element one (FE model) for the additional shot-peening parameters (Table 6) not used in the training.*

Figure 11 shows the change in the reduced parameters ( $\sigma_{max}$  and  $z_{aff}$ ) when the shot-peening parameters change their level for the reference shot-peening conditions:  $D=0.6\text{mm}$ ,  $V=70\times 10^3\text{mm/s}$ ,  $C=100\%$ ,  $\alpha=90^\circ$ . The finite element results are also presented in the Figure (squares) and it can be seen that the ANN predictions are in good agreement with the finite element ones. For the selected reference shot-peening conditions, the shot diameter, the shot velocity, and the impact angle have a significant effect on the affected depth  $z_{aff}$  as observed in the literature [26]. The increase of coverage increases slightly the affected depth  $z_{aff}$ . The shot diameter has almost no effect on the maximal compressive residual stress. The ANN model shows that the compressive stress is moderately affected by the impact velocity, which is also the case for the FE analysis in the present condition. Increasing the coverage and the impact angle close to normal shots ( $90^\circ$ ) results in an increase of the compressive stress.

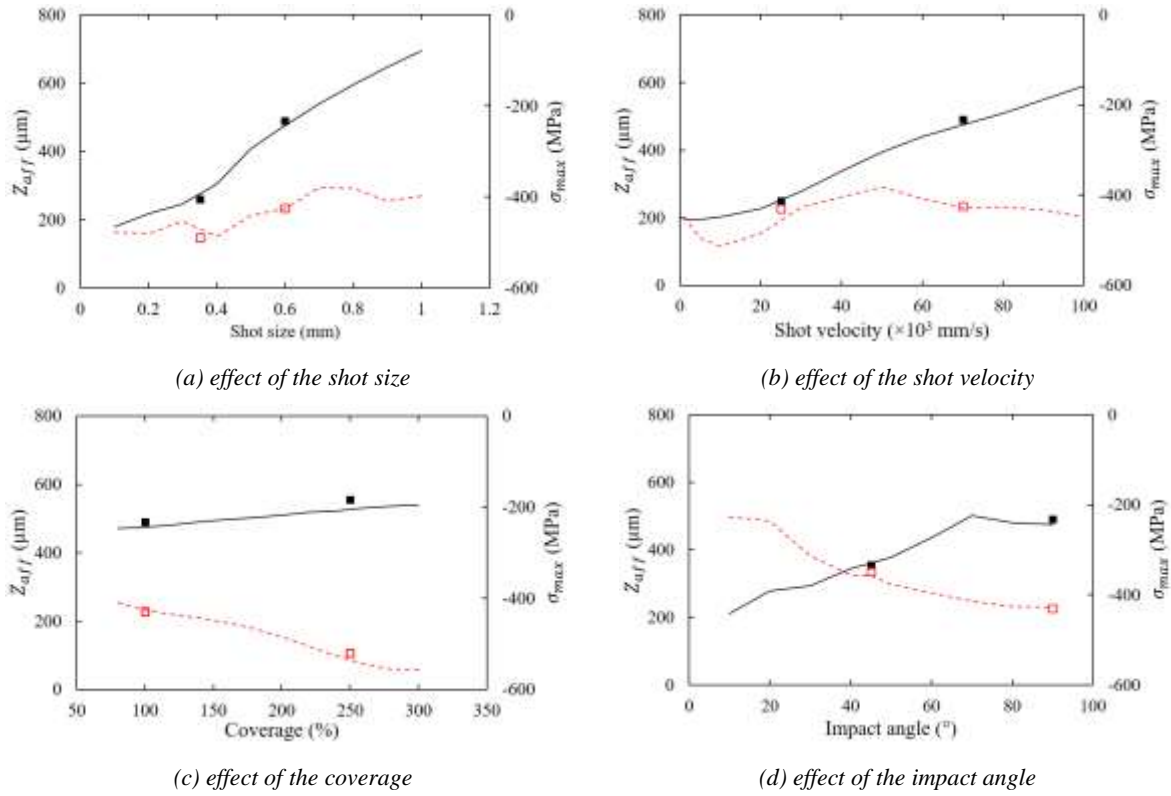


Figure 11 ANN model (25 neurons) – Effect of the process parameters on the reduced parameters of the residual stress profile: Affected depth  $z_{aff}$  (plain), maximal compressive stress  $\sigma_{max}$  (dashed), finite element results (Squares). Reference shot-peening condition:  $D=0.6\text{mm}$ ,  $V=70\times 10^3\text{mm/s}$ ,  $C=100\%$ ,  $\alpha=90^\circ$ .

## 5. Conclusions

In this work, two predictive models were developed to evaluate the effects of shot peening parameters on the predicted residual stress profile within the shot peened surface of TRIP780 steel. The capability of these models to get a representative shot-peening was evaluated and discussed. The main conclusions are as follows:

- Two predictive models, based on response surface methodology and artificial neural networks, were developed. The former is a second-order model and the latter is a feed-forward artificial neural network model.
- Several finite element simulations were conducted using a 3D multiple-impacts model coupled to central composite design of experiments. With the nonlinear combined isotropic/kinematic hardening law, adopted in the 3D multiple-impacts model to represent the macroscopic cyclic behavior of the target TRIP780 steel grade, it comparatively gives a good prediction of the residual stress profiles.

- A parametric analysis was conducted to underline the effect of the shot diameter, the shot velocity, the coverage, and the impact angle on the residual stress profiles.
- The high value of the regression coefficients found indicate that the second-order models can adequately predict the residual stress profiles.
- Results showed that the ANN predictions with 25 neurons and one single layer are in good agreement with the finite element ones.

It is worth outlining that the ANN model has the advantage to be applied to larger set of data, that would include the complete residual stress tensor, the plastic strain tensor, and the microgeometry obtained from the FE analysis. The developed predictive models have the advantages of a shorter time response that is highly suitable for active control of the process parameters. In the light of the obtained results, the proposed hybrid approach can be used in shot-peening optimization and extended to predict other mechanical multiaxial fields.

### **Acknowledgements**

This work was conducted with the help of the French Technological Research Institute for Materials, Metallurgy and Processes (IRT M2P). The authors would like to acknowledge IRT- M2P and the partners of the project CONDOR led by IRT M2P. The authors would like to acknowledge Mr. Fabien Caylus for his help on the ANN program.

## References

- [1] Y. X. Chen, J. C. Wang, Y. K. Gao, and A. H. Feng, "Effect of shot peening on fatigue performance of Ti2AlNb intermetallic alloy," *Int. J. Fatigue*, 2019.
- [2] W. C. Liu, J. Dong, P. Zhang, A. M. Korsunsky, X. Song, and W. J. Ding, "Improvement of fatigue properties by shot peening for Mg–10Gd–3Y alloys under different conditions," *Mater. Sci. Eng. A*, vol. 528, no. 18, pp. 5935–5944, 2011.
- [3] B. Bhuvvaraghan, S. M. Srinivasan, and B. Maffeo, "Optimization of the fatigue strength of materials due to shot peening: a survey," *Int. J. Struct. Chang. Solids*, vol. 2, no. 2, pp. 33–63, 2010.
- [4] S. Bagherifard, I. Fernandez-Pariente, R. Ghelichi, and M. Guagliano, "Effect of severe shot peening on microstructure and fatigue strength of cast iron," *Int. J. Fatigue*, vol. 65, pp. 64–70, 2014.
- [5] H. Wohlfahrt, "The influence of peening conditions on the resulting distribution of residual stress," in *Proceedings of the Second International Conference on Shot Peening*, 1984, pp. 316–331.
- [6] O. Vohringer, "Changes in the state of the material by shot peening," *ICSP3*, vol. 185, 1987.
- [7] M. Lundberg, R. L. Peng, M. Ahmad, T. Vuoristo, D. Bäckström, and S. Johansson, "Influence of shot peening parameters on residual stresses in flake and vermicular cast irons," in *Materials science forum*, 2014, vol. 768, pp. 534–541.
- [8] V. Llana and F. J. Belzunce, "Study of the effects produced by shot peening on the surface of quenched and tempered steels: roughness, residual stresses and work hardening," *Appl. Surf. Sci.*, vol. 356, pp. 475–485, 2015.
- [9] E. Nordin and B. Alfredsson, "Experimental Investigation of Shot Peening on Case Hardened SS2506 Gear Steel," *Exp. Tech.*, vol. 41, no. 4, pp. 433–451, 2017.
- [10] D. Wu, C. Yao, and D. Zhang, "Surface characterization of Ti1023 alloy shot peened by cast steel and ceramic shot," *Adv. Mech. Eng.*, vol. 9, no. 10, p. 1687814017723287, 2017.
- [11] A. Sorsa, S. Santa-aho, J. Warttinen, L. Suominen, M. Vippola, and K. Leiviskä, "Effect of shot peening parameters to residual stress profiles and Barkhausen noise," *J. Nondestruct. Eval.*, vol. 37, no. 1, p. 10, 2018.
- [12] M. Chen *et al.*, "Evaluation of the residual stress and microstructure character in SAF 2507 duplex stainless steel after multiple shot peening process," *Surf. Coatings Technol.*, vol. 344, pp. 132–140, 2018.
- [13] F. Petit-Renaud, J. T. Evans, A. V Metcalfe, and B. A. Shaw, "Optimization of a shot peening process," *Proc. Inst. Mech. Eng. Part L J. Mater. Des. Appl.*, vol. 222, no. 4, pp. 277–289, 2008.
- [14] Y.-S. Nam, Y.-I. Jeong, B.-C. Shin, and J.-H. Byun, "Enhancing surface layer properties of an aircraft aluminum alloy by shot peening using response surface methodology," *Mater. Des.*, vol. 83, pp. 566–576, 2015.
- [15] H. Y. Miao, S. Larose, C. Perron, and M. Lévesque, "An analytical approach to relate shot peening parameters to Almen intensity," *Surf. Coatings Technol.*, vol. 205, no. 7, pp. 2055–2066, 2010.
- [16] K. Sherafatnia, G. H. Farrahi, and A. H. Mahmoudi, "Effect of initial surface treatment on shot peening residual stress field: Analytical approach with experimental verification," *Int. J. Mech. Sci.*, vol. 137, pp. 171–181, 2018.
- [17] D. Gallitelli, J. Badreddine, E. Rouhaud, M. Micoulaut, C. Labergere, and M. Francois, "From process parameters to residual stress field: complete ultrasonic shot peening simulation," in *9th International Conference on Residual Stresses (ICRS-9)*, , October

- 2012, 2012.
- [18] D. Gallitelli *et al.*, “Simulation of shot peening: From process parameters to residual stress fields in a structure,” *Comptes Rendus Mécanique*, vol. 344, no. 4, pp. 355–374, 2016.
  - [19] J. Zarka, “Non-destructive testing method for determining a body’s mechanical properties and stresses.” Google Patents, 20-Jul-1976.
  - [20] G. Inglebert, “Analyse simplifiée des structures élasto-visco-plastiques sous chargements cycliques,” Arts et Métiers ParisTech, 1984.
  - [21] X. Liu, J. Liu, Z. Zuo, and H. Zhang, “Numerical study on residual stress redistribution of shot-peened aluminum 7075-T6 under fretting loading,” *Int. J. Mech. Sci.*, vol. 160, pp. 156–164, 2019.
  - [22] M. Guagliano, “Relating Almen intensity to residual stresses induced by shot peening: a numerical approach,” *J. Mater. Process. Technol.*, vol. 110, no. 3, pp. 277–286, 2001.
  - [23] J. Schwarzer, V. Schulze, and O. Vohringer, “Finite element simulation of shot peening-a method to evaluate the influence of peening parameters on surface characteristics,” in *Proceedings from International Conference of shot peening*, 2002, vol. 8.
  - [24] B. Bhuvaraghan, S. M. Srinivasan, B. Maffeo, and O. Prakash, “Constrained probabilistic multi-objective optimization of shot peening process,” *Eng. Optim.*, vol. 43, no. 6, pp. 657–673, 2011.
  - [25] T. Hong, J. Y. Ooi, and B. A. Shaw, “A numerical study of the residual stress pattern from single shot impacting on a metallic component,” *Adv. Eng. Softw.*, vol. 39, no. 9, pp. 743–756, 2008.
  - [26] L. Xie *et al.*, “Numerical analysis and experimental validation on residual stress distribution of titanium matrix composite after shot peening treatment,” *Mech. Mater.*, vol. 99, pp. 2–8, 2016.
  - [27] A. Ghasemi, S. M. Hassani-Gangaraj, A. H. Mahmoudi, G. H. Farrahi, and M. Guagliano, “Shot peening coverage effect on residual stress profile by FE random impact analysis,” *Surf. Eng.*, vol. 32, no. 11, pp. 861–870, 2016.
  - [28] Y. Zhang, F. Lai, S. Qu, V. Ji, H. Liu, and X. Li, “Effect of shot peening on residual stress distribution and tribological behaviors of 17Cr2Ni2MoVNB steel,” *Surf. Coatings Technol.*, vol. 386, p. 125497, 2020.
  - [29] T. Hong, J. Y. Ooi, and B. Shaw, “A numerical simulation to relate the shot peening parameters to the induced residual stresses,” *Eng. Fail. Anal.*, vol. 15, no. 8, pp. 1097–1110, 2008.
  - [30] T. Kim, H. Lee, H. C. Hyun, and S. Jung, “Effects of Rayleigh damping, friction and rate-dependency on 3D residual stress simulation of angled shot peening,” *Mater. Des.*, vol. 46, pp. 26–37, 2013.
  - [31] B. Bhuvaraghan, S. M. Srinivasan, and B. Maffeo, “Numerical simulation of Almen strip response due to random impacts with strain-rate effects,” *Int. J. Mech. Sci.*, vol. 53, no. 6, pp. 417–424, 2011.
  - [32] A. Burgold, M. Droste, A. Seupel, M. Budnitzki, H. Biermann, and M. Kuna, “Modeling of the cyclic deformation behavior of austenitic TRIP-steels,” *Int. J. Plast.*, vol. 133, p. 102792, 2020.
  - [33] A. Seupel and M. Kuna, “Application of a Local Continuum Damage Model to Porous TRIP-Steel,” in *Applied Mechanics and Materials*, 2015, vol. 784, pp. 484–491.
  - [34] H. Hallberg, P. Håkansson, and M. Ristinmaa, “A constitutive model for the formation of martensite in austenitic steels under large strain plasticity,” *Int. J. Plast.*, vol. 23, no. 7, pp. 1213–1239, 2007.
  - [35] P. Fu, K. Zhan, and C. Jiang, “Micro-structure and surface layer properties of

- 18CrNiMo7-6 steel after multistep shot peening,” *Mater. Des.*, vol. 51, pp. 309–314, 2013.
- [36] G. Fargas, J. J. Roa, and A. Mateo, “Effect of shot peening on metastable austenitic stainless steels,” *Mater. Sci. Eng. A*, vol. 641, pp. 290–296, 2015.
  - [37] X. Kleber and S. P. Barroso, “Investigation of shot-peened austenitic stainless steel 304L by means of magnetic Barkhausen noise,” *Mater. Sci. Eng. A*, vol. 527, no. 21–22, pp. 6046–6052, 2010.
  - [38] R. Guiheux, S. Berveiller, R. Kubler, D. Bouscaud, E. Patoor, and Q. Puydt, “Martensitic transformation induced by single shot peening in a metastable austenitic stainless steel 301LN: Experiments and numerical simulation,” *J. Mater. Process. Technol.*, vol. 249, pp. 339–349, 2017.
  - [39] R. F. Kubler, S. Berveiller, D. Bouscaud, R. Guiheux, E. Patoor, and Q. Puydt, “Shot peening of TRIP780 steel: Experimental analysis and numerical simulation,” *J. Mater. Process. Technol.*, vol. 270, pp. 182–194, 2019.
  - [40] M. Halilović, S. Issa, M. Wallin, H. Hallberg, and M. Ristinmaa, “Prediction of the residual state in 304 austenitic steel after laser shock peening – Effects of plastic deformation and martensitic phase transformation,” *Int. J. Mech. Sci.*, vol. 111–112, pp. 24–34, 2016.
  - [41] R. F. Kubler, M. Berveiller, and P. Buessler, “Semi phenomenological modelling of the behavior of TRIP steels,” *Int. J. Plast.*, vol. 27, no. 3, pp. 299–327, 2011.
  - [42] Z. Chen, Z. Sun, and B. Panicaud, “Constitutive modeling of TWIP/TRIP steels and numerical simulation of single impact during Surface Mechanical Attrition Treatment,” *Mech. Mater.*, vol. 122, pp. 69–75, 2018.
  - [43] M. J. Afzal, F. Maqbool, R. Hajavifard, J. Buhl, F. Walther, and M. Bambach, “Modeling the Residual Stresses Induced in the Metastable Austenitic Stainless Steel Disc Springs manufactured by Incremental Sheet Forming by a Combined Hardening Model with Phase Transformation,” *Procedia Manuf.*, vol. 47, pp. 1410–1415, 2020.
  - [44] M. Zimmermann, M. Klemenz, and V. Schulze, “Literature review on shot peening simulation,” *Int. J. Comput. Mater. Sci. Surf. Eng.*, vol. 3, no. 4, pp. 289–310, 2010.
  - [45] N. Harsha, I. A. Kumar, K. S. R. Raju, and S. Rajesh, “Prediction of Machinability characteristics of Ti6Al4V alloy using Neural Networks and Neuro-Fuzzy techniques,” *Mater. Today Proc.*, vol. 5, no. 2, Part 2, pp. 8454–8463, 2018.
  - [46] F. Abbassi, T. Belhadj, S. Mistou, and A. Zghal, “Parameter identification of a mechanical ductile damage using Artificial Neural Networks in sheet metal forming,” *Mater. Des.*, vol. 45, pp. 605–615, 2013.
  - [47] S. D. Kumar, K. Purushothaman, D. Chandramohan, M. M. Dushyantraj, and T. Sathish, “ANN-AGCS for the prediction of temperature distribution and required energy in hot forging process using finite element analysis,” *Mater. Today Proc.*, vol. 21, pp. 263–267, 2020.
  - [48] L. Li and S. Anand, “Hatch pattern based inherent strain prediction using neural networks for powder bed fusion additive manufacturing,” *J. Manuf. Process.*, 2020.
  - [49] E. Maleki and G. H. Farrahi, “Modelling of conventional and severe shot peening influence on properties of high carbon steel via artificial neural network,” *Int. J. Eng.*, vol. 31, no. 2, pp. 382–393, 2018.
  - [50] E. Maleki and K. Sherafatnia, “Investigation of single and dual step shot peening effects on mechanical and metallurgical properties of 18CrNiMo7-6 steel using artificial neural network,” *Int. J. Mater. Mech. Manuf.*, vol. 4, pp. 100–105, 2016.
  - [51] O. Unal and E. Maleki, “Shot peening optimization with complex decision-making tool: Multi criteria decision-making,” *Measurement*, vol. 125, pp. 133–141, 2018.
  - [52] L. SUN, M. LI, and H. LI, “Prediction model for surface layer microhardness of

- processed TC17 via high energy shot peening,” *Trans. Nonferrous Met. Soc. China*, vol. 27, no. 9, pp. 1956–1963, 2017.
- [53] D. C. Montgomery, *Design and analysis of experiments*. John Wiley & sons, 2017.
  - [54] E. Maleki, O. Unal, and K. R. Kashyzadeh, “Fatigue behavior prediction and analysis of shot peened mild carbon steels,” *Int. J. Fatigue*, vol. 116, pp. 48–67, 2018.
  - [55] J.-L. Chaboche, “A review of some plasticity and viscoplasticity constitutive theories,” *Int. J. Plast.*, vol. 24, no. 10, pp. 1642–1693, 2008.
  - [56] J. S. Novak and D. Benasciutti, “Parameter estimation of cyclic plasticity models and strain-based fatigue curves in numerical analysis of mechanical components under thermal loads,” *Cited pages i, xi*, vol. 3, no. 5, p. 6, 2016.
  - [57] P. Sanjurjo, C. Rodriguez, I. Penuelas, T. E. Garcia, and F. J. Belzunce, “Influence of the target material constitutive model on the numerical simulation of a shot peening process,” *Surf. Coatings Technol.*, vol. 258, pp. 822–831, 2014.
  - [58] R. Fathallah, “Modélisation du procédé de grenaillage incidence des billes et taux de recouvrement,” Paris, ENSAM, 1994.
  - [59] H. Ziegler, “A modification of Prager’s hardening rule,” *Q. Appl. Math.*, vol. 17, no. 1, pp. 55–65, 1959.
  - [60] W. Prager, “A new methods of analyzing stresses and strains in work hardening plastic solids,” *J. Appl. Mech.(ASME)*, vol. 23, pp. 493–496, 1956.
  - [61] R. Foerch, J. Besson, G. Cailletaud, and P. Pilvin, “Polymorphic constitutive equations in finite element codes,” *Comput. Methods Appl. Mech. Eng.*, vol. 141, no. 3–4, pp. 355–372, 1997.
  - [62] Dassault-Systemes, “ABAQUS software,” 2019.
  - [63] V. Boyer, “Modélisation du grenaillage d'un alliage de nickel avec prise en compte de l'écrouissage et de la microstructure.” Troyes, 2017.
  - [64] H. Hertz, “Ueber die Berührung fester elastischer Körper.,” *J. für die reine und Angew. Math.*, vol. 1882, no. 92, pp. 156–171, 1882.
  - [65] K. L. Johnson and K. L. Johnson, *Contact mechanics*. Cambridge university press, 1987.
  - [66] W. Johnson, “Impact Strength of Materials,|| Edward Arnold Publishers LTD,” London, UK, 1972.
  - [67] P. Renaud, “Modélisation numérique du grenaillage des pièces initialement cémentées ou carbonitrurées,” École Nationale Supérieure d’Arts et Métiers, 2011.
  - [68] M. T. Rahmaan, “Low to high strain rate characterization of DP600, TRIP780, AA5182-O.” University of Waterloo, 2015.
  - [69] F. Pedregosa *et al.*, “Scikit-learn: Machine learning in Python,” *J. Mach. Learn. Res.*, vol. 12, pp. 2825–2830, 2011.
  - [70] D. P. Kingma and J. Ba, “Adam: A method for stochastic optimization,” *arXiv Prepr. arXiv1412.6980*, 2014.